Editors' Suggestion

Strain-Enhanced Spin Readout Contrast in Silicon Carbide Membranes

Haibo Hu[1,2,*] Guodong Bian[3,*] Ailun Yi,[4,5,*] Chunhui Jiang,[1] Junhua Tan,[1] Qi Luo[1] Bo Liang,[1] Zhengtong Liu[2] Xinfang Nie[6,7] Dawei Lu,[6,7] Shumin Xiao,[1,2,7,8] Xin Ou,[4,5,†] Ádám Gali[3,9,10,‡] Yu Zhou,[1,7,§] and Qinghai Song[1,2,7,8,‖]

[1]*Ministry of Industry and Information Technology Key Lab of Micro-Nano Optoelectronic Information System,*
Guangdong Provincial Key Laboratory of Semiconductor Optoelectronic Materials and Intelligent Photonic Systems,
Harbin Institute of Technology, Shenzhen 518055, People's Republic of China
[2]*Pengcheng Laboratory, Shenzhen 518055, People's Republic of China*
[3]*HUN-REN Wigner Research Centre for Physics, Institute for Solid State Physics and Optics, P.O. Box 49, H-1525, Budapest, Hungary*
[4]*State Key Laboratory of Materials for Integrated Circuits, Shanghai Institute of Microsystem and Information Technology,*
Chinese Academy of Sciences, Shanghai 200050, People's Republic of China
[5]*The Center of Materials Science and Optoelectronics Engineering, University of Chinese Academy of Sciences,*
Beijing 100049, People's Republic of China
[6]*Department of Physics, State Key Laboratory of Quantum Functional Materials,*
and Guangdong Basic Research Center of Excellence for Quantum Science,
Southern University of Science and Technology, Shenzhen 518055, China
[7]*Quantum Science Center of Guangdong-HongKong-Macao Greater Bay Area (Guangdong), Shenzhen 518045, China*
[8]*Collaborative Innovation Center of Extreme Optics, Shanxi University, Taiyuan 030006, Shanxi, People's Republic of China*
[9]*Department of Atomic Physics, Institute of Physics, Budapest University of Technology and Economics,*
Műegyetem rakpart 3, 1111 Budapest, Hungary
[10]*MTA-WFK Lendület "Momentum" Semiconductor Nanostructures Research Group, P.O. Box 49, H-1525, Budapest, Hungary*

Quantum defects in solids have emerged as a transformative platform for advancing quantum technologies. A key requirement for these applications is achieving high-fidelity single-spin readout, particularly at room temperature for quantum biosensing. Here, we demonstrate through *ab initio* simulations of a primary quantum defect in 4H silicon carbide that strain is an effective control parameter for significantly enhancing readout contrast. We validate this principle experimentally by inducing local strain in silicon carbide-on-insulator membranes, achieving a readout contrast exceeding 60% while preserving the favorable coherence properties of single spins. Our findings establish strain engineering as a powerful strategy for optimizing coherent spin-photon interfaces in PL6 divacancy centers within silicon carbide membranes and potentially other similar defect systems.

Introduction—Quantum defects in solid-state materials have emerged as promising platforms for advancing quantum technologies [1–4]. A central requirement for these applications is the ability to efficiently initialize, manipulate, and read out spin states with high fidelity [5]. Among these processes, optical spin readout contrast—the relative difference in photon counts between distinct spin states—is essential for ensuring the efficiency and reliability of quantum operations [6–10]. Low optical spin readout contrast significantly limits sensitivity in quantum metrology [5] and restricts the feasibility of single-shot readout [9,11–13]. Although substantial progress has been made in improving optical readout contrast at cryogenic temperatures through spin-to-charge conversion or resonant excitations [7,9,12–14], at room temperature, the maximum achievable optical spin readout contrast remains at much lower values [5,8,15,16]. Recently, optical pulse sequences have been optimized to increase the optical spin readout contrast for nitrogen-vacancy (NV) centers in diamond [17]; nevertheless, the maximum readout contrast is still fundamentally limited by the inherent properties of the color centers that govern spin-selective fluorescence and optical spin polarization. This limitation underscores the need for novel strategies to enhance the off-resonant optical spin readout contrast for specific defect types and drive advancements in quantum technologies.

In principle, the spin readout contrast of isolated solid-state spin-defect systems depends on the critical rates in the optical spin-polarization loop [18] involving radiative and intersystem crossing (ISC) transitions. The relative strength between radiative and ISC processes primarily governs

---

*These authors contributed equally to this work.
†Contact author: ouxin@mail.sim.ac.cn
‡Contact author: gali.adam@wigner.hun-ren.hu
§Contact author: zhouyu2022@hit.edu.cn
‖Contact author: qinghai.song@hit.edu.cn

spin-dependent fluorescence emission, and the rates of ISC transitions are significantly influenced by variations in spin-state energy gaps and spin-orbit coupling (SOC) [19–21]. However, the feasible methods for modulating radiative and ISC rates to improve spin readout contrast remain largely unexplored. As a result, a significant gap exists in the experimental enhancement of optical spin readout contrast through emission and ISC engineering in solid-state quantum defect systems.

In this Letter, we introduce a comprehensive theoretical framework for analyzing strain-mediated modulation of radiative and ISC rates. Using first-principles calculations, we show that appropriate strain fields can significantly enhance the optical spin readout contrast of divacancy qubits in 4H-silicon carbide (SiC). Experimentally, we harness longitudinal strain in 4H-SiC membranes and achieve a 60.6% off-resonant optical spin readout contrast for divacancy qubits at room temperature. These results may suggest that strain engineering could be a promising strategy for optimizing coherent spin-photon interfaces in SiC and other wide-band-gap semiconductor platforms.

ZFS, ZPL, and readout contrast calculation—The effects of strain on the zero-field splitting (ZFS) and zero-phonon line (ZPL) of the well-studied *hh*-divacancy center in 4H-SiC [22] were investigated using first-principles methods (see Supplemental Material for details [23]). Figure 1(a) shows the lattice distortion
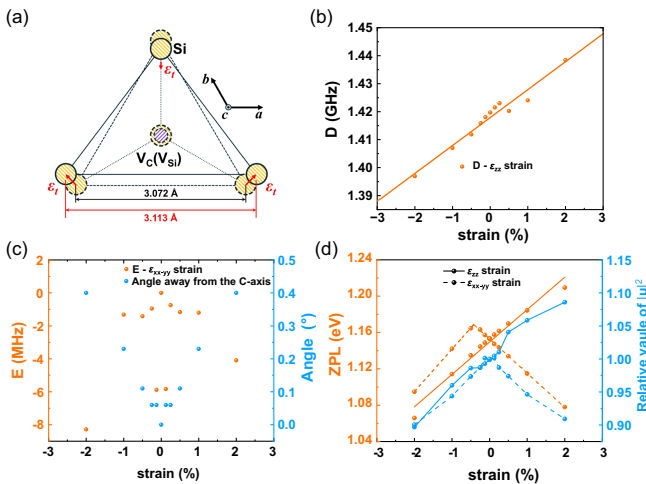
FIG. 1. (a) Schematic diagram of the change of *hh* divacancy due to the transverse strain ε_{xx-yy}. The *c* axis is perpendicular to the paper and extends outward. All yellow (purple) striped filled spheres represent Si (C) atoms. The dotted (solid) outline indicates the absence (presence) of strain. The black and red number with a unit of Å shows the distance between the two Si atoms neighboring the divacancy before and after applying the 1% tensile transverse strain. (b) Calculated D parameters under longitudinal strains. (c) Calculated E parameters (orange) and the angle away from the c axis (blue) under transverse strains. (d) Calculated ZPL values (orange) and relative values of $|\boldsymbol{\mu}|^2$ (blue) under both longitudinal and transverse strains.

induced by 1% transverse strain, corresponding to a 0.041 Å change in the distance between the nearest two Si atoms. We explored both longitudinal (ε_{zz}) and transverse (ε_{xx-yy}) strains, the latter lowering the symmetry from C_{3v} to C_{1h} [35]. Our calculations show that ε_{zz} primarily tunes the axial ZFS parameter D linearly, while ε_{xx-yy} mainly induces a nonzero E term [Figs. 1(b) and 1(c)]. Both strain components shift the ZPL energy, with ε_{zz} causing a significant linear shift [≈ 35.7 meV/(% strain)] consistent with trends in diamond NV centers [36] [Fig. 1(d)]. Strain also modulates the radiative rate k_{rad} through its dependence on the ZPL frequency ν and transition dipole moment $|\boldsymbol{\mu}|^2$ [Fig. 1(d)], as described in Ref. [37]:

$$k_{\text{rad}} = \frac{n(2\pi)^3 \nu^3 |\boldsymbol{\mu}|^2}{3\epsilon_0 h c^3},\tag{1}$$

where n is the refractive index of 4H-SiC [37], ν is the ZPL transition frequency, $\boldsymbol{\mu}$ is the transition dipole moment, ϵ_0 is the vacuum permittivity, h is the Planck constant, and c is the speed of light in vacuum. From Eq. (1), k_{rad} is proportional to both $|\boldsymbol{\mu}|^2$ and ν^3. The relative values of $|\boldsymbol{\mu}|^2$ are shown in Fig. 1(d), alongside the corresponding ZPL values (i.e., ν). Small jumps in D, E, ZPL, and $|\boldsymbol{\mu}|^2$ observed in Fig. 1 are attributed to numerical noise arising from the limited precision of first-principles calculations for small strains (up to 2%) and related postprocessing procedures such as spin decontamination and diagonalization.

Next, the effect of strain on the spin readout contrast is analyzed. Figure 2(a) displays our five-level rate-equation model with the major associated rates, which are categorized into radiative transitions (with rates of k_{31} and k_{42}, where $k_{31} = k_{42} = k_{\text{rad}}$) and nonradiative ISC transitions (with rates of k_{35}, k_{45}, k_{51}, and k_{52}). The relationship between k_{rad} and strain has been previously discussed. The singlet-triplet ISC rates k_{51} and k_{52} play a role in the perfect optical spin polarization into the $m_s = 0$ ground state, and their strain response is a second-order process [21]. Thus, their role in the optical cycle remains unchanged under strain, allowing us to adopt the same assumptions for pulsed optically detected magnetic resonance (ODMR) contrast C as stated in Ref. [16], expressed as

$$C = \frac{\tau_{-1} - \tau_0}{\tau_0} = \frac{k_0 - k_{-1}}{k_{-1}},\tag{2}$$

with $k_0 = 1/\tau_0 = k_{31} + k_{35}$ (where k_{35} is extremely weak to be ignored [16]) and $k_{-1} = 1/\tau_{-1} = k_{42} + k_{45}$, where τ_0 and τ_{-1} are the lifetimes of the excited states for $m_s = 0$ and $m_s = -1$, respectively. The ISC rate k_{45} mainly depends on the energy gap Δ between triplet excited state $|^3E\rangle$ and singlet state $|^1A_1\rangle$ and the SOC term [19–21]. Figure 2(b) displays the calculated Δ and SOC results under various strains. As the longitudinal strain increases (from negative to positive), the Δ values show an approximately linear
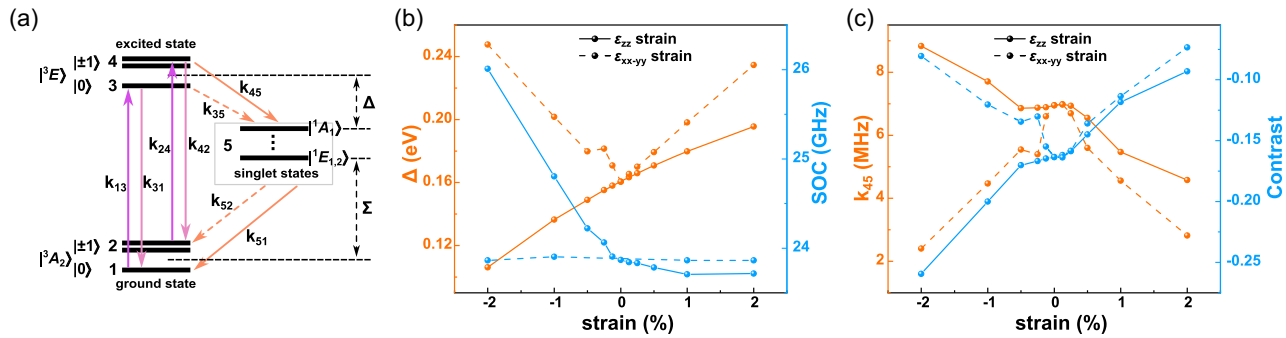
FIG. 2.   (a) Five-level model with major associated rates and energy gaps. Pink arrows indicate the radiative transition, and orange arrows indicate the strong (solid) and weak (dashed) nonradiative decay via the singlet states. k_{ij} ($i, j = 1, 2, 3, 4, 5$) are rates for these transitions. (b),(c) Calculated Δ, SOC, k_{45}, and contrast under various strains.

trend of change, with the value decreasing, while the SOC values show an exponential downward trend and seem to be converging. Under increasing the transverse strain, the Δ first decreases and then increases, showing a V-shaped trend, while SOC remains almost unchanged. Mapping these calculated Δ and SOC, all the k_{45} results are addressed and shown in Fig. 2(c). Finally, the effects of longitudinal and transverse strains on the contrast are calculated and presented in Fig. 2(c). Longitudinal strain primarily drives the enhancement of the contrast under lattice compression. The contrast becomes larger under the negative longitudinal strain of -2% and reaches a value of -25.9%, which finally leads to a 59% increase from the results without strain.

Spin and optical characterization of a single spin in silicon carbide on insulator (SiCOI)—Based on the above analysis, we have chosen SiCOI as the experimental framework for this study. This selection is primarily motivated by SiCOI's ability to generate a significant strain field with a dominant longitudinal compressive component, which is difficult to achieve in bulk SiC [38]. The fabrication process inevitably introduces some transverse strain due to lattice mismatch at the SiC/SiO$_2$ interface, but this is not an ideal or intentional aspect of our selection. We characterized a single PL6A divacancy spin in a 200-nm-thick SiCOI membrane [Fig. 3(a), inset]. The membrane was fabricated via a multistep thinning and polishing technique [39,40] that avoids ion-induced damage, with full process details provided in Supplemental Material [23]. This method inherently introduces significant interfacial strain—a combination of longitudinal (ε_{zz}) and transverse (ε_{xx-yy}) strain components—due to the lattice mismatch between SiC and SiO$_2$. Figure 3(a) displays the confocal scanning map of the single defect PL6 A in the membrane.

Under 914-nm continuous wave (cw) excitation, the defect's saturation curve [Fig. 3(b)], fitted with $I_P = I_s \cdot P(P + P_s)$, yields a saturation power P_s of 0.70(3) mW and intensity I_s of 119.8(13) kcps, a brightness comparable to bulk PL6 centers [16]. Single-photon

emission is confirmed by $g^2(0) \ll 0.5$ [16,41], obtained from the second-order correlation function $g^2(t)$ [Fig. 3(b), inset] after background correction with the formula $g^2(\tau) = [g^2_{\text{raw}}(\tau) - (1 - \rho^2)]/\rho^2$, where $\rho = s/(s + b)$ [42]. The defect's spectral fingerprint includes a 4 K ZPL at 1058.2 nm [Fig. 3(c)] and a two-peak ODMR spectrum [Fig. 3(d)]. Magnetic-field-dependent ODMR measurements further identified it as an axial divacancy (details in Supplemental Material [23]); the defect exhibits behavior characteristic of an axial divacancy. The spin Hamiltonian under strain [43] is

$$H = (D_{\text{gs}} + \Pi_z)S_z^2 + \Pi_x(S_yS_y - S_xS_x) + \gamma_eB_zS_z, \quad (3)$$

where D_{gs} is the ground state ZFS, $\Pi_{x/z}$ is the strain along the x/z axis, S is the electronic spin, γ_e is the gyromagnetic ratio of the electronic spin, and B_z is the z component of the external magnetic field. From the fitting with the total Hamiltonian, as displayed in Fig. S1(a) [23], the ZFS parameters $D = 1336.6(1)$ MHz and $E = 22.1(2)$ MHz were obtained. The strained defect exhibits a cw-ODMR contrast of $\sim 30\%$ under a magnetic field, significantly higher than the $\sim 15\%$ reported for bulk PL6 centers [16]. Pulsed measurements reveal a striking Rabi contrast of 60.6 (10)% [Fig. 3(e)], doubling the value from bulk SiC [16]. We attribute this dramatic enhancement to the large, localized strain in the SiCOI membrane modulating the defect's radiative and ISC rates. This interpretation is supported by characterization of multiple single spins across the sample, which show a consistent range of ZFS D parameters from 1336.54 to 1353.55 MHz [Fig. 3(f)]. Based on our calculations [Fig. 1(b)], this D range corresponds to a local strain of approximately -2%. Except for the 4 K PL and ZPL spectra [Figs. 3(c) and 3(f), respectively], all measurements were performed at room temperature.

Lacking a confirmed microscopic origin for PL6, we model its strain response using the PL1 divacancy, which shares the same symmetry and, thus, captures the key trends. After applying a constant offset of -26 MHz and -78 nm to align the calculated D and ZPL values with zero-strain
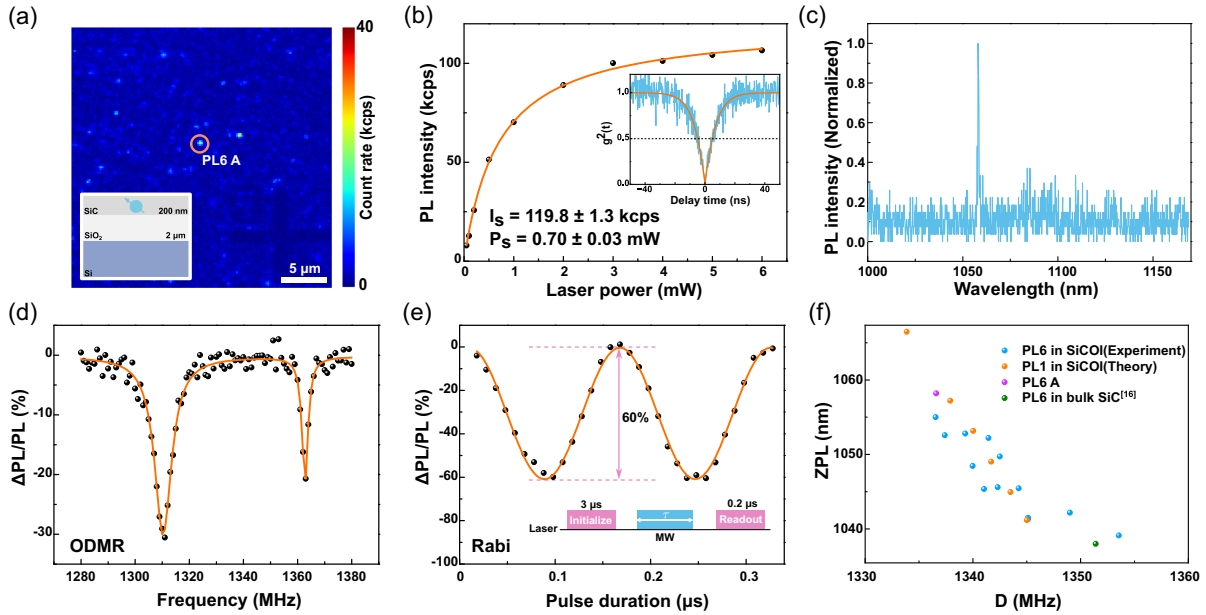
FIG. 3. Spin and optical properties of the single spin in SiCOI. (a) Confocal scanning image of the defect, with the inset showing a diagram of the cross-sectional view of the SiCOI sample. The SiC membrane has a thickness of 200 nm. (b) Saturation behavior. The black dots are the background-corrected experimental data, and the solid line is a fit using the function $I_P = I_s \cdot P(P + P_s)$, where P and I_P are the power of the excitation laser and the corresponding count rate, respectively. The inset is the second-order correlation function $g^2(t)$ measurement of the single spin. At an excitation laser power of 0.2 mW, $g^2(0)$ is well below 0.5, indicating single-photon emission. (c) Photoluminescence (PL) spectra of the single spin at 4 K reveal a ZPL peak near 1058.2 nm. (d) ODMR spectra of the single spin at zero magnetic fields show two prominent peaks. The black dots are the raw data, while the solid lines show the corresponding Lorentzian fits. (e) Rabi oscillations of the left peak in (d), the raw data were fitted with a cosine function, and the Rabi readout contrast is approximately $60.6 \pm (10)\%$. (f) Comparison of the relationship between ZPL and D for some strained defects with theoretical calculations.

experimental data, their strain dependence shows excellent agreement with theory [Figs. 1(b) and 1(d)]. This strong correspondence confirms that the high optical readout contrast originates from the large strain in the SiCOI.

Temporal dynamics and models of the spin readout process—To uncover the underlying spin dynamics, spin-resolved excited-state lifetime measurements were conducted at room temperature for the $m_s = 0$ and $m_s = -1$

states of the single PL6 A spin, as shown in Fig. 4(a). The orange and green lines illustrate the fitting with a double-exponential decay, in which the longer time parameters are lifetimes of $\tau_0 = 11.1(1)$ ns and $\tau_{-1} = 4.9(1)$ ns for $m_s = 0$ and $m_s = -1$, respectively, and the other fast decay may originate from the system response or background fluorescence decay [44]. These lifetimes offer valuable insights into the spin-state dynamics and excited-state
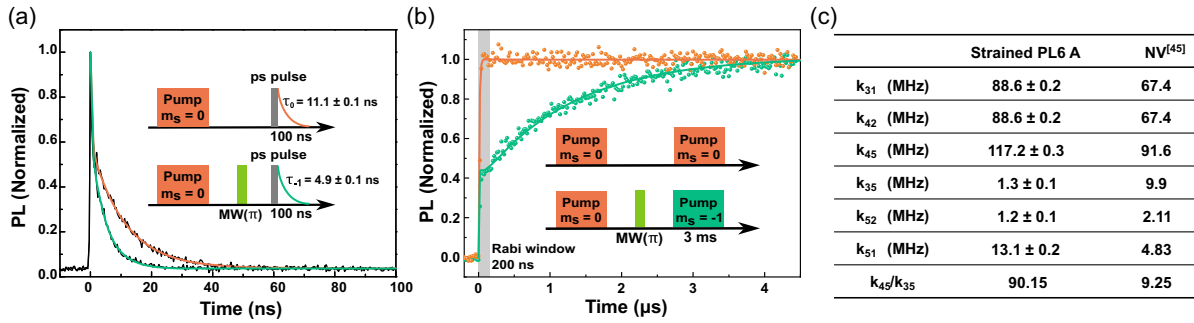
FIG. 4. (a) Spin-resolved excited-state lifetime measurements for the single PL6 A spin at $m_s = 0$ or $m_s = -1$ at room temperature. The orange and green lines are the double-exponential fitting, revealing a longer lifetime of 11.1(1) ns and 4.9(1) ns for $m_s = 0$ and $m_s = -1$, respectively, and a shorter decay from the system response or background fluorescence. (b) The fitting of the fluorescence traces for the single PL6 A spin at $m_s = 0$ and $m_s = -1$ with the model in Fig. 2(a). (c) Comparison of the parameters fitted by the level model for the strained single PL6 A spin with diamond NV center in Ref. [45]. All data here pertain to the single PL6 A.

decay processes, affecting the overall spin readout contrast. The C value of the strained PL6 A is calculated to be 56% using Eq. (2), compared with the value of 33.6% of PL6 in bulk SiC [16]. This value is close to the Rabi contrast of 60.6%, which we obtained experimentally in Fig. 3(e). Furthermore, we measured additional single-color centers (PL6 B–PL6 E) (Supplemental Material [23]) and observed a Rabi contrast ranging from 21% to 43%. Notably, as the Rabi contrast increased, the ratio of $C = (\tau_{-1} - \tau_0)/\tau_0$ also decreased, and these two values are close in magnitude (Fig. S3 [23]), consistent with the above analysis.

Besides direct lifetime measurement, we further explore the dynamics of the spin readout by performing time-resolved fluorescence measurements for the strained PL6 A, as depicted in Fig. 4(b). The fluorescence traces following optical initialization ($m_s = 0$) are compared with and without applying a microwave π pulse to flip the spin state. The gray-shaded region indicates the Rabi window, corresponding to the photon accumulation time ($\tau = 200$ ns) used for Rabi oscillation in Fig. 3(e). The time window's duration is crucial for maximizing the contrast of the spin readout. A shorter time window yields fewer photons per cycle, requiring a balance between time resolution and photon count. For diamond NV centers, the optimal duration for this window is approximately 220 ns [8,46]. Another factor affecting the Rabi contrast is the excitation power. An increase in applied power leads to a faster spin initialization, which, in turn, results in a decrease in Rabi contrast, as detailed in Supplemental Material [23].

The time-resolved fluorescence dynamics were quantitatively analyzed using our five-level rate equation model [Fig. 2(a)], with the spin-dependent lifetimes from Fig. 4(a) serving as critical constraints, as detailed in Supplemental Material [23]. All fitting parameters obtained are compared with those from the well-studied NV center in diamond [45], as shown in Fig. 4(c). The ratio of $k_{51}/k_{52} > 10$—resulting in a nearly perfect optical spin polarization—and the relation of $k_{35} \ll k_{45}$ validate our initial assumption. A prominent feature emerges in the strained PL6 system, where the k_{45}/k_{35} ratio demonstrates approximately tenfold enhancement compared to the NV center, directly mirroring our first-principles predictions of strain-reduced energy gaps Δ between the triplet excited state $|^3E\rangle$ and singlet ground state $|^1A_1\rangle$ [18]. This quantitative agreement bridges microscopic strain effects with macroscopic contrast improvement, where the 60.6% Rabi contrast [Fig. 3(e)] emerges as a direct consequence of accelerated ISC transitions under compressive strain, as evidenced by the synergy between theoretical modeling and experimental observations.

Discussion and outlook—Our combined theoretical and experimental study demonstrates that strain in the SiC membrane effectively modulates ISC transition rates, with axial strain playing a key role in enhancing nonradiative ISC pathways. Additionally, we experimentally achieve a spin readout contrast exceeding 60% in strained SiCOI

membranes. These results establish strain engineering as a versatile strategy for enhancing spin readout contrast in PL6 centers, a principle with potential applications for other defects in platforms such as 2D materials and diamond membranes [47,48].

[1] I. Aharonovich, D. Englund, and M. Toth, Solid-state single-photon emitters, Nat. Photonics **10**, 631 (2016).

[2] M. Atatüre, D. Englund, N. Vamivakas, S.-Y. Lee, and J. Wrachtrup, Material platforms for spin-based photonic quantum technologies, Nat. Rev. Mater. **3**, 38 (2018).

[3] G. Wolfowicz, F. J. Heremans, C. P. Anderson, S. Kanai, H. Seo, A. Gali, G. Galli, and D. D. Awschalom, Quantum guidelines for solid-state spin defects, Nat. Rev. Mater. **6,** 906 (2021).

[4] Q.-Y. Luo, Q. Li, J.-F. Wang, P.-J. Guo, W.-X. Lin, S. Zhao, Q.-C. Hu, Z.-Q. Zhu, J.-S. Xu, C.-F. Li *et al.*, Fabrication and quantum sensing of spin defects in silicon carbide, Front. Phys. **11,** 1270602 (2023).

[5] J. F. Barry, J. M. Schloss, E. Bauch, M. J. Turner, C. A. Hart, L. M. Pham, and R. L. Walsworth, Sensitivity optimization for NV-diamond magnetometry, Rev. Mod. Phys. **92,** 015004 (2020).

[6] L. J. Rogers, K. D. Jahnke, M. H. Metsch, A. Sipahigil, J. M. Binder, T. Teraji, H. Sumiya, J. Isoya, M. D. Lukin, P. Hemmer *et al.*, All-optical initialization, readout, and coherent preparation of single silicon-vacancy spins in diamond, Phys. Rev. Lett. **113,** 263602 (2014).

[7] P. Neumann, J. Beck, M. Steiner, F. Rempp, H. Fedder, P. R. Hemmer, J. Wrachtrup, and F. Jelezko, Single-shot readout of a single nuclear spin, Science **329,** 542 (2010).

[8] D. A. Hopper, H. J. Shulevitz, and L. C. Bassett, Spin readout techniques of the nitrogen-vacancy center in diamond, Micromachines **9,** 437 (2018).

[9] X.-Y. Lai, R.-Z. Fang, T. Li, R.-Z. Su, J. Huang, H. Li, L.-X. You, X.-H. Bao, and J.-W. Pan, Single-shot readout of a nuclear spin in silicon carbide, Phys. Rev. Lett. **132,** 180803 (2024).

[10] M. Gulka, D. Wirtitsch, V. Ivády, J. Vodnik, J. Hruby, G. Magchiels, E. Bourgeois, A. Gali, M. Trupke, and M. Nesladek, Room-temperature control and electrical readout of individual nitrogen-vacancy nuclear spins, Nat. Commun. **12,** 4421 (2021).

[11] A. Delteil, W.-b. Gao, P. Fallahi, J. Miguel-Sanchez, and A. Imamoğlu, Observation of quantum jumps of a single quantum dot spin using submicrosecond single-shot optical readout, Phys. Rev. Lett. **112,** 116802 (2014).

[12] Q. Zhang, Y. Guo, W. Ji, M. Wang, J. Yin, F. Kong, Y. Lin, C. Yin, F. Shi, Y. Wang *et al.*, High-fidelity single-shot readout of single electron spin in diamond with spin-to-charge conversion, Nat. Commun. **12,** 1529 (2021).

[13] C. P. Anderson, E. O. Glen, C. Zeledon, A. Bourassa, Y. Jin, Y. Zhu, C. Vorwerk, A. L. Crook, H. Abe, J. Ul-Hassan *et al.*, Five-second coherence of a single spin with single-shot readout in silicon carbide, Sci. Adv. **8,** eabm5912 (2022).

[14] N. Aslam, G. Waldherr, P. Neumann, F. Jelezko, and J. Wrachtrup, Photo-induced ionization dynamics of the nitrogen vacancy defect in diamond investigated by single-shot charge state detection, New J. Phys. **15,** 013064 (2013).

[15] J.-C. Jaskula, B. J. Shields, E. Bauch, M. D. Lukin, A. S. Trifonov, and R. L. Walsworth, Improved quantum sensing with a single solid-state spin via spin-to-charge conversion, Phys. Rev. Appl. **11,** 064003 (2019).

[16] Q. Li, J.-F. Wang, F.-F. Yan, J.-Y. Zhou, H.-F. Wang, H. Liu, L.-P. Guo, X. Zhou, A. Gali, Z.-H. Liu *et al.*, Room-temperature coherent manipulation of single-spin qubits in silicon carbide with a high readout contrast, Natl. Sci. Rev. **9,** nwab122 (2022).

[17] D. Wirtitsch, G. Wachter, S. Reisenbauer, M. Gulka, V. Ivády, F. Jelezko, A. Gali, M. Nesladek, and M. Trupke, Exploiting ionization dynamics in the nitrogen vacancy center for rapid, high-contrast spin, and charge state initialization, Phys. Rev. Res. **5,** 013014 (2023).

[18] G. Bian, G. Thiering, and Á. Gali, Theory of optical spin-polarization of axial divacancy and nitrogen-vacancy defects in 4H-SiC, Phys. Rev. Res. **7,** 013320 (2025).

[19] M. L. Goldman, M. Doherty, A. Sipahigil, N. Y. Yao, S. Bennett, N. Manson, A. Kubanek, and M. D. Lukin, State-selective intersystem crossing in nitrogen-vacancy centers, Phys. Rev. B **91,** 165201 (2015).

[20] G. Thiering and A. Gali, *Ab initio* calculation of spin-orbit coupling for an NV center in diamond exhibiting dynamic Jahn-Teller effect, Phys. Rev. B **96,** 081115(R) (2017).

[21] G. Thiering and A. Gali, Theory of the optical spin-polarization loop of the nitrogen-vacancy center in diamond, Phys. Rev. B **98,** 085207 (2018).

[22] W. F. Koehl, B. B. Buckley, F. J. Heremans, G. Calusine, and D. D. Awschalom, Room temperature coherent control of defect spin qubits in silicon carbide, Nature (London) **479,** 84 (2011).

[23] See Supplemental Material at http://link.aps.org/supplemental/10.1103/tdb3-tqfv, for extra theoretical derivations, numerical simulations, and experimental method, which includes Refs. [24–34].

[24] J. Paier, M. Marsman, K. Hummer, G. Kresse, I. C. Gerber, and J. G. Ángyán, Screened hybrid density functionals applied to solids, J. Chem. Phys. **124,** 154709 (2006).

[25] G. Kresse and J. Furthmüller, Efficiency of ab-initio total energy calculations for metals and semiconductors using a plane-wave basis set, Comput. Mater. Sci. **6,** 15 (1996).

[26] G. Kresse and J. Hafner, *Ab initio* molecular dynamics for liquid metals, Phys. Rev. B **47,** 558 (1993).

[27] G. Kresse and J. Furthmüller, Efficient iterative schemes for *ab initio* total-energy calculations using a plane-wave basis set, Phys. Rev. B **54,** 11169 (1996).

[28] P. Deák, B. Aradi, T. Frauenheim, E. Janzén, and A. Gali, Accurate defect levels obtained from the HSE06 range-separated hybrid functional, Phys. Rev. B **81,** 153203 (2010).

[29] A. V. Krukau, O. A. Vydrov, A. F. Izmaylov, and G. E. Scuseria, Influence of the exchange screening parameter on the performance of screened hybrid functionals, J. Chem. Phys. **125,** 224106 (2006).

[30] J. Heyd, G. E. Scuseria, and M. Ernzerhof, Hybrid functionals based on a screened Coulomb potential, J. Chem. Phys. **118,** 8207 (2003).

[31] Z. Bodrog and A. Gali, The spin–spin zero-field splitting tensor in the projector-augmented-wave method, J. Phys. Condens. Matter **26,** 015305 (2013).

[32] T. Biktagirov, W. G. Schmidt, and U. Gerstmann, Spin decontamination for magnetic dipolar coupling calculations: Application to high-spin molecules and solid-state spin qubits, Phys. Rev. Res. **2,** 022024(R) (2020).

[33] S. Steiner, S. Khmelevskyi, M. Marsmann, and G. Kresse, Calculation of the magnetic anisotropy with projected-augmented-wave methodology and the case study of disordered $Fe_{1-x}Co_x$ alloys, Phys. Rev. B **93,** 224425 (2016).

[34] A. Gali, E. Janzén, P. Deák, G. Kresse, and E. Kaxiras, Theory of spin-conserving excitation of the $N-V^-$ center in diamond, Phys. Rev. Lett. **103,** 186404 (2009).

[35] P. Udvarhelyi and A. Gali, *Ab initio* spin-strain coupling parameters of divacancy qubits in silicon carbide, Phys. Rev. Appl. **10**, 054010 (2018).

[36] G. I. López-Morales, J. M. Zajac, J. Flick, C. A. Meriles, and C. E. Dreyer, Quantum embedding study of strain-and electric-field-induced stark effects on the NV⁻ center in diamond, Phys. Rev. B **110**, 245127 (2024).

[37] J. Davidsson, Theoretical polarization of zero phonon lines in point defects, J. Phys. Condens. Matter **32**, 385502 (2020).

[38] A. L. Falk, P. V. Klimov, B. B. Buckley, V. Ivády, I. A. Abrikosov, G. Calusine, W. F. Koehl, Á. Gali, and D. D. Awschalom, Electrically and mechanically tunable electron spins in silicon carbide color centers, Phys. Rev. Lett. **112**, 187601 (2014).

[39] D. M. Lukin, C. Dory, M. A. Guidry, K. Y. Yang, S. D. Mishra, R. Trivedi, M. Radulaski, S. Sun, D. Vercruysse, G. H. Ahn *et al.*, 4H-silicon-carbide-on-insulator for integrated quantum and nonlinear photonics, Nat. Photonics **14**, 330 (2020).

[40] H. Hu, Y. Zhou, A. Yi, T. Bao, C. Liu, Q. Luo, Y. Zhang, Z. Wang, Q. Li, D. Lu *et al.*, Room-temperature waveguide integrated quantum register in a semiconductor photonic platform, Nat. Commun. **15**, 10256 (2024).

[41] A. L. Falk, B. B. Buckley, G. Calusine, W. F. Koehl, V. V. Dobrovitski, A. Politi, C. A. Zorman, P. X.-L. Feng, and D. D. Awschalom, Polytype control of spin qubits in silicon carbide, Nat. Commun. **4**, 1819 (2013).

[42] J. Wang, Y. Zhou, Z. Wang, A. Rasmita, J. Yang, X. Li, H. J. von Bardeleben, and W. Gao, Bright room temperature single photon source at telecom range in cubic silicon carbide, Nat. Commun. **9**, 4106 (2018).

[43] N. Wang, C.-F. Liu, J.-W. Fan, X. Feng, W.-H. Leong, A. Finkler, A. Denisenko, J. Wrachtrup, Q. Li, and R.-B. Liu, Zero-field magnetometry using hyperfine-biased nitrogen-vacancy centers near diamond surfaces, Phys. Rev. Res. **4**, 013098 (2022).

[44] D. J. Christle, P. V. Klimov, C. F. de las Casas, K. Szász, V. Ivády, V. Jokubavicius, J. Ul Hassan, M. Syväjärvi, W. F. Koehl, T. Ohshima *et al.*, Isolated spin qubits in SiC with a high-fidelity infrared spin-to-photon interface, Phys. Rev. X **7**, 021046 (2017).

[45] A. Gupta, L. Hacquebard, and L. Childress, Efficient signal processing for time-resolved fluorescence detection of nitrogen-vacancy spins in diamond, J. Opt. Soc. Am. B **33**, B28 (2016).

[46] M. W. Doherty, N. B. Manson, P. Delaney, F. Jelezko, J. Wrachtrup, and L. C. Hollenberg, The nitrogen-vacancy colour centre in diamond, Phys. Rep. **528**, 1 (2013).

[47] J. Jing, F. Sun, Z. Wang, L. Ma, Y. Luo, Z. Du, T. Zhang, Y. Wang, F. Xu, T. Zhang *et al.*, Scalable production of ultraflat and ultraflexible diamond membrane, Nature (London) **636**, 627 (2024).

[48] X. Guo, M. Xie, A. Addhya, A. Linder, U. Zvi, S. Wang, X. Yu, T. D. Deshmukh, Y. Liu, I. N. Hammock *et al.*, Direct-bonded diamond membranes for heterogeneous quantum and electronic technologies, Nat. Commun. **15**, 8788 (2024).